Crystal structures of K2[XSi5O12] (X = Fe2+, Co, Zn) and Rb2[XSi5O12] (X = Mn) leucites: comparison of monoclinic P21/c and Iad polymorph structures and inverse relationship between tetrahedral cation (T = Si and X)—O bond distances and intertetrahedral T—O—T angles

BELL, Anthony and HENDERSON, C. Michael B.

Published version

BELL, Anthony and HENDERSON, C. Michael B. (2018). Crystal structures of K2[XSi5O12] (X = Fe2+, Co, Zn) and Rb2[XSi5O12] (X = Mn) leucites: comparison of monoclinic P21/c and Iad polymorph structures and inverse relationship between tetrahedral cation (T = Si and X)—O bond distances and intertetrahedral T—O—T angles. Acta crystallographica Section B, Structural science, crystal engineering and materials, 74 (3), 274-286.

Acta Cryst B
STRUCTURAL SCIENCE
CRYSTAL ENGINEERING
MATERIALS
ISSN 2052-5206

Crystal structures of $K_2[XSi_5O_{12}]$ (X = Fe^{2+}, Co, Zn) and $Rb_2[XSi_5O_{12}]$ (X = Mn) leucites: comparison of monoclinic $P2_1/c$ and $Ia\bar{3}d$ polymorph structures and inverse relationship between tetrahedral cation (T = Si and X)—O bond distances and intertetrahedral T—O—T angles

Received 19 January 2018
Accepted 9 March 2018

Edited by S. Parsons, University of Edinburgh, Scotland

Keywords: X-ray powder diffraction; Rietveld refinement; leucite-group minerals; silicate framework structures.

Supporting information: this article has supporting information at journals.iucr.org/b

Anthony M. T. Bell[a]* **and C. Michael B. Henderson**[b,c]

[a]Materials and Engineering Research Institute (MERI), Sheffield Hallam University, Sheffield, S1 1WB, UK, [b]School of Earth and Environmental Sciences, University of Manchester, Manchester, M13 9PL, UK, and [c]ASTeC, Sci-Tech Daresbury Laboratory, Science and Technology Facilities Council, Warrington, WA4 4AD, UK. *Correspondence e-mail: anthony.bell@shu.ac.uk

The leucite tectosilicate mineral analogues $K_2X^{2+}Si_5O_{12}$ (X = Fe^{2+}, Co, Zn) and $Rb_2X^{2+}Si_5O_{12}$ (X = Mn) have been synthesized at elevated temperatures both dry at atmospheric pressure and at controlled water vapour pressure; for X = Co and Zn both dry and hydrothermally synthesized samples are available. Rietveld refinement of X-ray data for hydrothermal $K_2X^{2+}Si_5O_{12}$ (X = Fe^{2+}, Co, Zn) samples shows that they crystallize in the monoclinic space group $P2_1/c$ and have tetrahedral cations (Si and X) ordered onto distinct framework sites [*cf.* hydrothermal $K_2MgSi_5O_{12}$; Bell *et al.* (1994*a*), *Acta Cryst.* B**50**, 560–566]. Dry-synthesized $K_2X^{2+}Si_5O_{12}$ (X = Co, Zn) and $Rb_2X^{2+}Si_5O_{12}$ (X = Mn) samples crystallize in the cubic space group $Ia\bar{3}d$ and with Si and X cations disordered in the tetrahedral framework sites as typified by dry $K_2MgSi_5O_{12}$. Both structure types have tetrahedrally coordinated SiO_4 and XO_4 sharing corners to form a partially substituted silicate framework. Extraframework K^+ and Rb^+ cations occupy large channels in the framework. Structural data for the ordered samples show that mean tetrahedral Si—O and X—O bond lengths cover the ranges 1.60 Å (Si—O) to 2.24 Å (Fe^{2+}—O) and show an inverse relationship with the intertetrahedral angles (T—O—T) which range from 144.7° (Si—O—Si) to 124.6° (Si—O—Fe^{2+}). For the compositions with both disordered and ordered tetrahedral cation structures ($K_2MgSi_5O_{12}$, $K_2CoSi_5O_{12}$, $K_2ZnSi_5O_{12}$, $Rb_2MnSi_5O_{12}$ and $Cs_2CuSi_5O_{12}$ leucites) the disordered polymorphs always have larger unit-cell volumes, larger intertetrahedral T—O—T angles and smaller mean T—O distances than their isochemical ordered polymorphs. The ordered samples clearly have more flexible frameworks than the disordered structures which allow the former to undergo a greater degree of tetrahedral collapse around the interframework cavity cations. Multivariant linear regression has been used to develop equations to predict intertetrahedral T—O—T angle variation depending on the independent variables Si—O and X—O bond lengths, cavity cation ideal radius, intratetrahedral (O—T—O) angle variance, and X cation electronegativity.

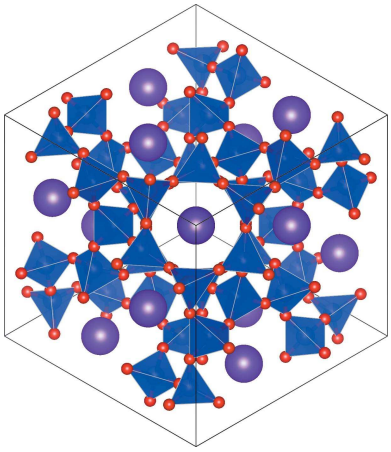

1. Introduction

The naturally occurring tectosilicate minerals leucite ($K[AlSi_2O_6]$; Mazzi *et al.*, 1976), pollucite ($Cs[AlSi_2O_6]$; Yanase *et al.*, 1997), analcime ($Na[AlSi_2O_6]\cdot H_2O$; Ferraris *et al.*, 1972) and kirchoffite ($Cs[BSi_2O_6]$; Agakhanov *et al.*, 2012) have the same ideal three-dimensional tetrahedrally coordinated structure-type (square brackets define the framework stoichiometry). This structure type has been described as the

ANA structure (Baerlocher *et al.*, 2001) and consists of tetrahedra linked to form four rings which in turn are linked to form six rings defining regular non-intersecting channels parallel to the [111] crystallographic direction. Interframework (cavity) cations (*A*-site cations) occupying these channels include large K, Rb, Cs and NH_4^+ in leucites and pollucites, and also molecular water in analcime. These non-intersecting channels interconnect along independent [110] directions to form distorted eight-membered tetrahedral rings defining *S* cation sites which are occupied by Na in analcime. A very wide range of synthetic samples of phases having the basic ANA structure with large cations occupying *A* sites is known; the most significant series in our present research has divalent cations and extra Si replacing Al cations in the framework (*i.e.* $X + Si \leftrightarrow 2Al$; Torres-Martinez & West, 1989) to produce samples having the anhydrous general formula $A_2X^{2+}Si_5O_{12}$ (*A* = K, Rb, Cs and *X* = Mg, Mn, Fe^{2+}, Co, Ni, Cu, Cd, Zn). The aluminosilicate phases usually have tetragonal ($I4_1/a$) or cubic ($Ia\bar{3}d$) space groups with disordered tetrahedral cations but the phases containing divalent cations can occur either with cubic $Ia\bar{3}d$ (disordered framework cations) or as orthorhombic *Pbca* and monoclinic $P2_1/c$ (ordered framework cations) phases. Over the whole range of leucite-type phases, space groups adopted include $I4_1/a$, $Ia\bar{3}d$, $I4_1/acd$, $I\bar{4}3d$, $Pa\bar{3}$, *Pbca* and $P2_1/c$; all are isotropy subgroups of the aristotype phase belonging to the space group $Ia\bar{3}d$. Distortions from the ideal cubic structure tend to be restricted and all phases can be considered on the basis of a 'pseudocubic' $Ia\bar{3}d$ cell [see Henderson *et al.* (2017) and the review contained within].

In these leucite structures the alkali metal *A* cations sit in the extraframework channels. Ion exchange can be used to remove these extraframework cations which makes them of technological interest as a possible storage medium for radioactive Cs from nuclear waste (Gatta *et al.*, 2008*a*).

As part of a wider attempt to understand the consequences of tetrahedral ordering in framework silicates, we report here structural data for hydrothermally synthesized phases having the monoclinic $P2_1/c$ space group typified by $K_2MgSi_5O_{12}$ (Bell *et al.*, 1994*a*); these have the compositions $K_2Fe^{2+}Si_5O_{12}$, $K_2CoSi_5O_{12}$ and $K_2ZnSi_5O_{12}$. The last two compositions are also available as dry-synthesized cubic $Ia\bar{3}d$ polymorphs [*cf.* $K_2MgSi_5O_{12}$; Bell *et al.* (1994*a*)] and the structures of these along with cubic $Rb_2MnSi_5O_{12}$ are also reported. Wider structural properties are discussed based on the new data and those for the most reliable structures from the $A_2X^{2+}Si_5O_{12}$ database (Bell *et al.*, 1994*a*,*b*, 2010; Bell & Henderson, 1996, 2016; Henderson *et al.*, 1998; 2017).

2. Experimental methods

2.1. Sample synthesis

The samples were synthesized by the procedures summarized by Henderson *et al.* (2016). Starting glass compositions were prepared in a standard muffle furnace in air (100 kPa) as follows: *X* = Co, 1473 K for 1.5 h; *X* = Zn, 1373 K for 0.5 h; $RbMnSi_5O_{12}$, 1573 K for 2 h. Melts were quenched by dipping the bottoms of the Pt crucibles in water.

The starting glass for the *X* = Fe sample was initially prepared from a mixture melted in air at 1523 K, 100 kPa, $10^{-0.68}$ atm oxygen for two days. This oxidized glass was reduced in a gas-mixing furnace at 1473 K, 100 kPa, 10^{-10} atm oxygen, 16 h and then crystallized hydrothermally in a cold-seal pressure vessel at 883 K with 50 MPa water pressure for 11 days (sample HF2L3). To ensure that Fe was fully reduced to Fe^{2+}, HF2L3 was heated in a sealed quartz glass tube in the presence of the Fe–FeO buffer at 1073 K and 10^{-20} atm oxygen for 3 h. Preparation of Co leucites was also not straightforward as Henderson *et al.* (2016) reported that $K_2CoSi_5O_{12}$ leucite could not be synthesized dry at 1 bar; this comment reflected that a considerable amount of glass was always present. The 'dry' sample used here does indeed contain glass but Henderson *et al.* (2016) showed that near-edge XANES structures of glass and dry-crystallized leucites are identical, implying the presence of identical short-range order in both materials. The hydrothermally crystallized Co leucite contained a small amount of a mica-like impurity which could have the stoichiometry $KCo_3^{2+}[Co^{3+}Si_3O_{10}](OH)_2$ (similar to $KCo_3^{2+}[Al^{3+}Si_3O_{10}](OH)_2$; Redhammer & Roth, 2002). Such a phase indicates that the hydrothermal leucite could also contain some Co^{3+}; however, the XANES spectrum and refined EXAFS Co—O first-shell distance (1.96 Å) are both typical of tetrahedral Co^{2+} as the dominant species. We conclude that both Co-leucite phases are close to the expected stoichiometry, *i.e.* $K_2Co^{2+}Si_5O_{12}$.

2.2. X-ray powder diffraction method

For the ambient-temperature X-ray powder diffraction studies all samples were mounted on low-background silicon wafers. The hydrothermal *X* = Fe sample and the dry *X* = Zn and *X* = Mn samples were studied using a PANalytical X'Pert Pro MPD diffractometer with Cu *Kα* X-rays, fixed divergence slits and an PANalytical X'Celerator area detector fitted with a graphite monochromator. The other three samples were studied with a PANalytical Empyrean diffractometer with a PIXcel^{3D} area detector. The hydrothermal *X* = Zn sample data were collected using Cu *Kα* X-rays and the Co samples were studied with Co *Kα* X-rays. Programmable divergence slits were used for the *X* = Zn samples and fixed divergence slits for both *X* = Co samples. Powder diffraction data were analysed using the Rietveld (1969) method. Further experimental details are given in Table 1; note that the high-χ^2 value for the hydrothermal *X* = Zn sample was due to the unnecessarily long data collection time (over the weekend) for this sample.

Fig. 1 shows the diffraction data displayed as a Rietveld difference plot for the hydrothermal *X* = Fe sample [structure (III)]; one diffraction peak at 17.18° 2θ could not be indexed as a leucite peak. Fig. 2 shows data for the hydrothermal *X* = Zn sample [structure (IV)]; note that the anomalously high low-angle peak intensities reflect that the data collected using

Table 1
Experimental details.

For all structures: T = 293 K, Z = 8. For structures (I), (II) and (III): Cu $K\alpha$, λ = 1.540560 Å; PANalytical X'Pert Pro MPD diffractometer, flat plate specimen mounting, data collection mode scanning, scanning method continuous. For structures (IV), (V) and (VI): PANalytical Empyrean diffractometer, flat plate specimen mounting, data collection mode reflection, scanning method continuous.

	(I)	(II)	(III)
Crystal data			
Chemical formula	$K_2ZnSi_5O_{12}$ (dry)	$Rb_2MnSi_5O_{12}$ (dry)	$K_2FeSi_5O_{12}$ (hydrothermal)
M_r	476.00	557.92	466.46
Crystal system, space group	Cubic, $Ia\bar{3}d$	Cubic, $Ia\bar{3}d$	Monoclinic, $P2_1/c$
a, b, c (Å)	13.3772 (2), 13.3772 (2), 13.3772 (2)	13.5635 (3), 13.5635 (3), 13.5635 (3)	13.2574 (5), 13.6739 (6), 12.9240 (5)
α, β, γ (°)	90, 90, 90	90, 90, 90	90, 93.048 (3), 90
V (Å^3)	2393.87 (6)	2495.24 (10)	2339.54 (16)
Specimen shape, size (mm)	Irregular, 10 × 5 × 1	Irregular, 10 × 10 × 1	Irregular, 15 × 15 × 1
Data collection			
$2\theta_{min}$ (°)	15.04	15.28	4.95
$2\theta_{max}$ (°)	99.92	100.16	74.93
$2\theta_{step}$ (°)	0.0167	0.0167	0.0167
Total scan time (h)	16.6	10	19
Refinement			
R_p (%)	4.538	4.679	2.760
R_{wp} (%)	5.879	6.144	4.051
R_{exp} (%)	4.639	5.137	2.992
R_{Bragg} (%)	8.312	8.974	6.944
χ^2	1.606	1.431	1.834
No. of data points	5080	5080	4189
No. of parameters	43	38	169
No. of restraints	0	0	48

	(IV)	(V)	(VI)
Crystal data			
Chemical formula	$K_2ZnSi_5O_{12}$ (hydrothermal)	$K_2CoSi_5O_{12}$ (hydrothermal)	$K_2CoSi_5O_{12}$ (dry)
M_r	476.00	469.55	469.55
Crystal system, space group	Monoclinic, $P2_1/c$	Monoclinic, $P2_1/c$	Cubic, $Ia\bar{3}d$
a, b, c (Å)	13.1773 (2), 13.6106 (2), 13.0248 (2)	13.18783 (14), 13.63495 (16), 12.98764 (14)	13.3767 (3), 13.3767 (3), 13.3767 (3)
α, β, γ (°)	90, 91.6981 (9), 90	90, 91.9994 (8), 90	90, 90, 90
V (Å^3)	2334.98 (6)	2333.96 (4)	2393.57 (10)
Radiation type	Cu $K\alpha$, λ = 1.540560 Å	Co $K\alpha$, λ = 1.789190 Å	Co $K\alpha$, λ = 1.789190 Å
Specimen shape, size (mm)	Irregular, 10 × 5 × 1	Irregular, 10 × 10 × 1	Irregular, 10 × 5 × 1
Data collection			
2θ values (°)			
$2\theta_{min}$ (°)	4.96	8.28	18.28
$2\theta_{max}$ (°)	99.95	100.27	100.26
$2\theta_{step}$ (°)	0.0131	0.0131	0.0131
Total scan time (h)	63	19	17
Refinement			
R_p (%)	0.702	1.447	0.644
R_{wp} (%)	1.114	2.223	0.834
R_{exp} (%)	0.272	0.847	0.722
R_{Bragg} (%)	3.385	6.691	8.158
χ^2	16.817	6.895	1.334
No. of data points	7308	7007	6245
No. of parameters	179	169	57
No. of restraints	48	48	0

programmable divergence slits have been converted to intensities comparable to those obtained with fixed slits. Figs. 3, 5 and 6 show Rietveld difference plots for dry-synthesized X = Zn- [structure (I)], X = Co- [structure (VI)] and Rb_2- [structure (II)] $MnSi_5O_{12}$ leucites, respectively. The Rietveld difference plot for the hydrothermal X = Co sample [structure (V)] is displayed in Fig. 4 and shows the presence of peaks due to the presence of a micaceous impurity. Note the high background in Fig. 5 due to the presence of a significant glass component.

2.3. Powder pattern refinement

Samples of the hydrothermally synthesized X = Fe and Co had been loaded into borosilicate glass capillaries prior to synchrotron X-ray powder diffraction data collection using the

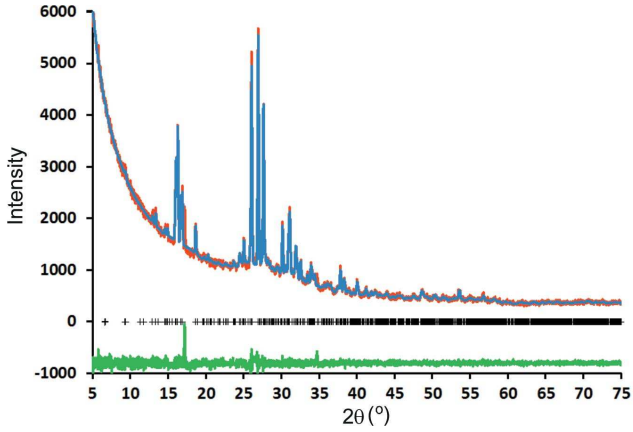

Figure 1
Rietveld difference plot for hydrothermally synthesized $K_2Fe^{2+}Si_5O_{12}$ [structure (III)]. Red line shows the observed powder diffraction plot, blue line shows the calculated powder diffraction plot, green line shows the difference between observed and calculated data, + symbols show the positions of the $P2_1/c$ Bragg reflections for $K_2Fe^{2+}Si_5O_{12}$.

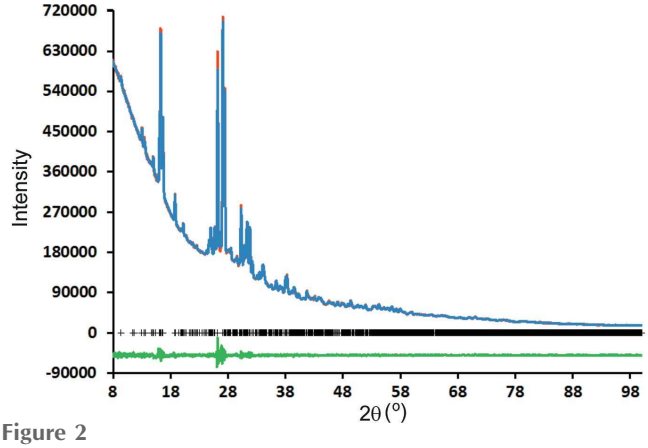

Figure 2
Rietveld difference plot for hydrothermally synthesized $K_2ZnSi_5O_{12}$ [structure (IV)]. Red line shows the observed powder diffraction plot, blue line shows the calculated powder diffraction plot, green line shows the difference between observed and calculated data, + symbols show the positions of the $P2_1/c$ Bragg reflections for $K_2ZnSi_5O_{12}$.

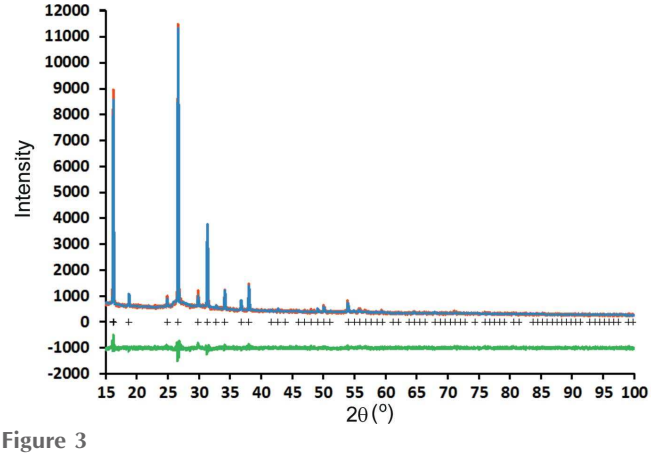

Figure 3
Rietveld difference plot for dry-synthesized $K_2ZnSi_5O_{12}$ [structure (I)]. Red line shows the observed powder diffraction plot, blue line shows the calculated powder diffraction plot, green line shows the difference between observed and calculated data, + symbols show the positions of the $Ia\bar{3}d$ Bragg reflections for $K_2ZnSi_5O_{12}$.

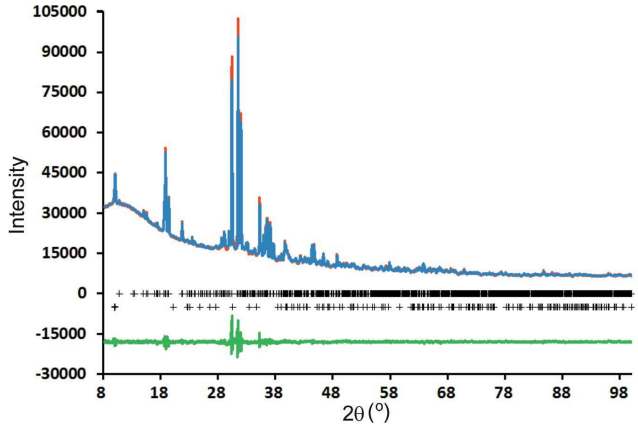

Figure 4
Rietveld difference plot for hydrothermally synthesized $K_2CoSi_5O_{12}$ [structure (V)]. Red line shows the observed powder diffraction plot, blue line shows the calculated powder diffraction plot, green line shows the difference between observed and calculated data. The upper + symbols show the positions of the $P2_1/c$ Bragg reflections for $K_2CoSi_5O_{12}$ and the lower + symbols show the positions for the mica impurity phase.

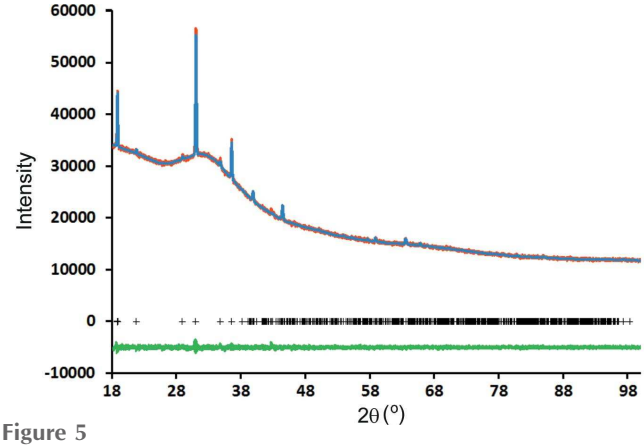

Figure 5
Rietveld difference plot for dry-synthesized $K_2CoSi_5O_{12}$ [structure (VI)]. Red line shows the observed powder diffraction plot, blue line shows the calculated powder diffraction plot, green line shows the difference between observed and calculated data. The + symbols show the positions of the $Ia\bar{3}d$ Bragg reflections for $K_2CoSi_5O_{12}$.

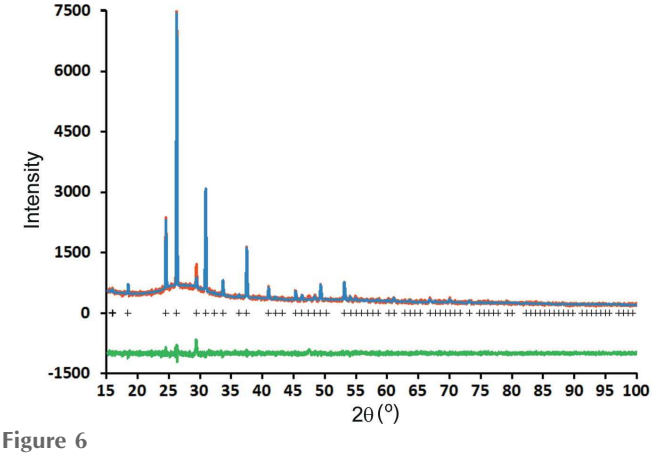

Figure 6
Rietveld difference plot for dry-synthesized $Rb_2MnSi_5O_{12}$ [structure (II)]. Red line shows the observed powder diffraction plot, blue line shows the calculated powder diffraction plot, green line shows the difference between observed and calculated data. The + symbols show the positions of the $Ia\bar{3}d$ Bragg reflections for $Rb_2MnSi_5O_{12}$.

Table 2
Comparison of crystal structure parameters for $K_2XSi_5O_{12}$ $P2_1/c$ leucite analogues with X = Mg, Fe^{2+}, Co and Zn, and with those for the *Pbca* analogues $Cs_2XSi_5O_{12}$ with X = Cu and Cd.

	$K_2MgSi_5O_{12}$ Bell *et al.* (1994*a*)	$K_2FeSi_5O_{12}$ This work	$K_2ZnSi_5O_{12}$ This work	$K_2CoSi_5O_{12}$ This work	$Cs_2CuSi_5O_{12}$ Bell *et al.* (2010)	$Cs_2CdSi_5O_{12}$ Bell *et al.* (1994*b*)
Space group	$P2_1/c$	$P2_1/c$	$P2_1/c$	$P2_1/c$	*Pbca*	*Pbca*
a (Å)	13.168 (5)	13.2574 (5)	13.1773 (2)	13.1878 (1)	13.58943 (6)	13.6714 (1)
b (Å)	13.652 (1)	13.6739 (6)	13.6106 (2)	13.6350 (2)	13.57355 (5)	13.8240 (1)
c (Å)	13.072 (5)	12.9240 (5)	13.0248 (2)	12.9876 (1)	13.62966 (4)	13.8939 (1)
β (°)	91.69 (5)	93.048 (3)	91.70 (6)	92.00 (1)	90	90
V (Å^3)	2348 (2)	2339.6 (2)	2334.98 (6)	2333.96 (4)	2512.847 (13)	2625.83 (6)
X^{2+} ionic radius† (Å)	0.57	0.63	0.60	0.58	0.57	0.78
Mean Si—O (Å)	1.62	1.62	1.61	1.63	1.615	1.60
Mean Q^4Si(4Si)—O (Å)	1.61	1.60	1.59	1.62	1.61	1.60
Mean X—O (Å)	1.90	1.96	1.89	1.93	1.914	2.24
Mean T—O (T = Si or X) (Å)	1.67	1.67	1.66	1.68	1.665	1.70
Mean K—O_6 (Å)	3.06	3.01	3.02	3.00	3.36	3.26
Mean K—O_{12} (Å)	3.35	3.35	3.36	3.31	3.46	3.50
Mean O—Q^4Si(4Si)—O variance (°)‡	11.9	192.6	45.3	59.0	19.1	44.7
Mean O—Q^4Si(3Si,1X)—O variance (°)‡	23.2	180.4	49.8	67.6	38.8	47.3
Mean O—Si—O variance (°)‡	20.9	183.1	48.5	65.9	34.9	46.8
Mean O—X—O variance (°)‡	40.4	230.3	62.6	75.3	159.4	94.2
Mean O—T—O variance (°)‡, (T = Si or X)	24.2	191	51.9	67.5	55.6	54.7
Mean Si—O—Si (°)	140.9	142.0	144.7	138.3	144.5	147
Mean Q^4Si(4Si)—O—Q^4Si(3Si,1X) (°)	140.8	142.7	145.5	138.2	144.1	145
Mean Si—O—X (°)	130.6	124.6	128.1	125.8	130.8	127
Mean T—O—T (°) (T = Si or X)	137.5	136.2	139.2	134.2	139.9	140.3
Mean predicted K—O_6 (Å)§	3.06	3.01	3.05	3.04	3.29	3.28
Mean predicted K—O_{12} (Å)§	3.34	3.33	3.33	3.33	3.44	3.48

† Shannon (1976). ‡ Robinson *et al.* (1971). § Henderson *et al.* (2017).

postal service for the I11 beamline (Thompson *et al.*, 2009) at Diamond Light Source. These data were all collected using a synchrotron X-ray wavelength of 0.825887 Å. Rietveld refinements were attempted using these data with the $P2_1/c$ structure of $K_2MgSi_5O_{12}$ (Bell *et al.*, 1994*a*) as a starting model and with Fe and Co respectively replacing Mg in the structures. However, it was not possible to satisfactorily refine the peak-shape parameters in these refinements. As a wavelength of 0.825887 Å had been used for data collection and due to the low symmetry of the $P2_1/c$ structures there were extreme peak overlaps. The $P2_1/c$ structure of $K_2MgSi_5O_{12}$ (Bell *et al.*, 1994*a*) was determined from synchrotron X-ray powder diffraction data collected at a wavelength of 1.52904 Å; in this case using a longer wavelength, extreme peak overlaps were not a problem. Therefore, Rietveld refinements for the hydrothermally synthesized X = Fe and Co samples were carried out using Cu $K\alpha$ (X = Fe) and Co $K\alpha$ (X = Co) X-ray powder diffraction data.

Analysis of the X-ray powder diffraction data for the hydrothermal X = Fe (apart from the unassigned peak at 17.18° 2θ) and X = Zn samples showed that all Bragg reflections could be indexed by a phase with similar cell parameters to those of the $P2_1/c$ tetrahedral cation-ordered structure of hydrothermally synthesized $K_2MgSi_5O_{12}$ (Bell *et al.*, 1994*a*). The main phase present in the hydrothermal X = Co sample also has this structure but a second, micaceous Co-phase (Redhammer & Roth, 2002), is present. Diffraction data for the dry-synthesized X = Zn, X = Co and $Rb_2MnSi_5O_{12}$ samples all have Bragg peaks that could be indexed as $Ia\bar{3}d$ phases similar to that of dry-synthesized $K_2MgSi_5O_{12}$ (Bell *et al.*, 1994*a*).

Rietveld refinements (Rietveld, 1969) were all carried out with *FULLPROF* (Rodríguez-Carvajal, 1993). In these refinements. the background correction was by linear interpolation between the refined intensities of background points measured in the powder diffraction data. A T-C-H profile function (van Laar & Yelon, 1984; Finger *et al.*, 1994); was used in these refinements. For the X = Zn samples, peak intensities were first converted in *High Score Plus* software (PANalytical, 2009) to be compatible with other data. For the hydrothermal X = Fe, Zn and Co refinements, the $P2_1/c$ structure of hydrothermal $K_2MgSi_5O_{12}$ was used as a starting structure with Fe, Zn or Co replacing Mg. Forty Si—O distances were restrained to those in the starting structure to ±0.02 Å. Eight X—O distances were similarly restrained to Mg—O distances in the starting structure (±0.02 Å) plus the respective differences between the ionic radii for Mg^{2+} and Fe^{2+}, Zn^{2+} or Co^{2+} (Shannon, 1976). For the hydrothermal X = Co sample the second phase was fitted with the $C2/m$ Co mica having the stoichiometry $KCo^{2+}[Co^{3+}Si_3O_{10}](OH_2)$ (Redhammer & Roth, 2002). Note that the $P2_1/c$ silicate framework structures of hydrothermal X = Fe, Zn and Co leucites all have Si and X ordered onto separate framework sites [ten Si and two X sites per formula unit (pfu)].

The Rietveld refinements for dry-synthesized X = Co and Zn and $Rb_2MnSi_5O_{12}$ leucites were all carried out using the $Ia\bar{3}d$ tetrahedral cation-disordered structure of dry-synthesized $K_2MgSi_5O_{12}$, with Co, Zn, and Mn replacing Mg, and Rb

Table 3
Comparison of crystal structure parameters for $A_2XSi_5O_{12}$ $Ia\bar{3}d$ leucite analogues having A = K and X = Mg, Co, and Zn with those for A = Rb and X = Mn and A = Cs and X = Cu.

	$K_2MgSi_5O_{12}$ Bell *et al.* (1994*a*)	$K_2CoSi_5O_{12}$ This work	$K_2ZnSi_5O_{12}$ This work	$Rb_2MnSi_5O_{12}$ This work	$Cs_2CuSi_5O_{12}$ Bell *et al.* (2010)
a (Å)	13.4190 (1)	13.3767 (3)	13.3772 (2)	13.5635 (3)	13.6322 (4)
V (Å^3)	2416.33 (5)	2393.57 (10)	2393.87 (6)	2495.24 (10)	2533.4 (2)
Mean T—O (Å) (T = Si and X)	1.610	1.65	1.61	1.65	1.642
Mean A—O_6 (Å)	3.339	3.297	3.338	3.308	3.363
Mean A—O_{12} (Å)	3.405	3.303	3.405	3.398	3.446
Mean O—T—O variance (°)†	10.7	106.5	10.6	48.5	21.7
Mean T—O—T angle (°)	144.5	135.3	144.5	139.4	142.9
Mean predicted A—O_6 (Å)‡	3.08	3.03	3.02	3.13	3.27
Mean predicted A—O_{12} (Å)§	3.39	3.37	3.37	3.42	3.47

† Robinson *et al.* (1971). ‡ Predicted from equation (5) (Henderson *et al.*, 2017). § From equation (6) (Henderson *et al.*, 2017).

Table 4
T—O—T bond angles (°) for $K_2XSi_5O_{12}$ (X = Fe, Zn, Co) $P2_1/c$ leucite structures.

	X = Fe	X = Zn	X = Co
Si2—O1—Si3	153 (2)	132 (1)	132 (2)
Si1—O2—Si4	136 (2)	152 (2)	144 (2)
Si4—O3—*X*6	126 (2)	133 (1)	130 (1)
Si3—O4—*X*5	120 (2)	116 (1)	111 (1)
Si2—O5—*X*5	119 (2)	125 (1)	125 (1)
Si1—O6—*X*6	123 (2)	122 (1)	126 (1)
*X*6—O7—Si7	115 (2)	139 (1)	131 (1)
Si2—O8—Si11	131 (2)	138 (1)	130 (2)
Si3—O9—Si12	129 (2)	167 (1)	150 (2)
*X*5—O10—Si10	122 (2)	119 (1)	123 (1)
Si1—O11—Si8	123 (2)	146 (1)	133 (2)
Si4—O12—Si9	159 (2)	151 (1)	139 (2)
Si8—O13—Si10	129 (2)	147 (1)	140 (1)
Si7—O14—Si11	159 (3)	148 (1)	139 (2)
Si11—O15—Si12	138 (2)	135 (1)	137 (2)
Si8—O16—Si9	154 (2)	139 (2)	135 (2)
Si9—O17—Si10	152 (2)	126 (1)	128 (2)
Si7—O18—Si12	124 (2)	141 (2)	128 (2)
Si1—O19—Si12	156 (2)	172 (2)	158 (2)
Si4—O20—Si10	138 (2)	135 (1)	135 (2)
*X*6—O21—Si8	150 (2)	152 (1)	141 (1)
Si2—O22—Si9	130 (2)	134 (2)	131 (2)
Si3—O23—Si7	162 (2)	153 (1)	155 (2)
*X*5—O24—Si11	121 (2)	118 (1)	119 (1)
Average angles			
Si—O—Si	142 (14)	145 (13)	138 (9)
Si—O—*X*	125 (11)	128 (13)	126 (9)
T—O—*T*	136 (15)	139 (15)	134 (11)
Si9—O—Si	149 (13)	137 (11)	133 (5)
Si12—O—Si	137 (14)	154 (19)	143 (14)

replacing K in the starting structures. Note that these framework structures all have Si and X cations disordered on a single tetrahedral site.

In the structural discussion we will be comparing these laboratory-based X-ray diffraction results with X-ray results on other samples obtained using synchrotron radiation (*e.g.* Bell *et al.*, 1994*a*,*b*; Bell & Henderson, 1996); the uncertainties on bond lengths and bond angles using the former are ~3 and ~5 times larger, respectively, than for the synchrotron data. Note also that our earlier combined synchrotron and neutron powder diffraction data for $Cs_2CuSi_5O_{12}$ (Bell *et al.*, 2010) has uncertainties ~25% smaller than of those found for purely synchrotron X-ray diffraction; of course this mainly reflects the much greater scattering of oxygen atoms with neutrons rather than X-rays. Thus although the present laboratory XRPD data have significantly higher uncertainties than our earlier data, we will be looking for similar structural trends to those found in our higher resolution experimental work, particularly the neutron diffraction results. Inevitably, the very large amount of sample required for neutron powder diffraction prohibited use of this technique for studying our scarce, difficult to synthesize, low-symmetry ($P2_1/c$) hydrothermal samples.

3. Results and discussion

X-ray powder diffraction data are displayed as Rietveld difference plots in Figs. 1 to 6; note the presence of an unassigned Bragg peak in the X = Fe sample (Fig. 1) and the presence of peaks for a minor micaceous impurity in the hydrothermal X = Co sample (Fig. 4). Table 1 shows the refined unit-cell parameters along with a summary of data collection information.

3.1. Space-group assignments and unit-cell parameters

The $P2_1/c$ monoclinic structures of $K_2XSi_5O_{12}$ (X = Fe, Zn, Co) leucites are all refined from the $P2_1/c$ structure of monoclinic hydrothermal $K_2MgSi_5O_{12}$ (Bell *et al.*, 1994*a*); this is the only published leucite structure with this space group. The Rietveld refinement of the X = Co phase was complicated by the presence of a Co-mica impurity which was included in the refinement as a minor phase; 4.7 (1) wt% was found to be present. All the $P2_1/c$ leucites have closely similar structures but the degree of framework distortion varies, mainly depending on the size of the divalent cation. The dry-synthesized X = Zn, X = Co and $Rb_2MnSi_5O_{12}$ leucites were all refined as cubic $Ia\bar{3}d$ by comparison with the structure of the dry-synthesized $K_2MgSi_5O_{12}$ (Bell *et al.*, 1994*a*); these cation-disordered leucites all have very similar structures with lattice parameters mainly depending on the sizes of the cavity cations (K^+ or Rb^+) and of the divalent cations.

Fig. 7 shows the principal topological features of the hydrothermal monoclinic $P2_1/c$ $K_2ZnSi_5O_{12}$ tetrahedrally ordered structure; in particular, how the primary building units (XO_4 tetrahedra) are linked to form the four-ring, six-

ring and eight-ring secondary building units (SBUs). Fig. 7(*c*) (down [001]) shows that the four rings close to this plane contain only Si tetrahedra all of which are linked to three other SiO_4 units and one ZnO_4 [*i.e.* denoted $Q^4Si(3Si, 1Zn)$]; linkages of different four-ring SBUs to form six rings are clear. Figs. 7(*a*) and 7(*b*) (down [100] and [010], respectively) show similar ring features but in both of these the four rings close to these planes contain two $Q^4Si(3Si, 1Zn)$ tetrahedra opposite each other, together with one $Q^4Si(4Si)$ and one $Q^4Zn(4Si)$ also at opposite corners. The fact that the ZnO_4 tetrahedron is significantly larger than the SiO_4 tetrahedra results in the four rings shown in Figs. 7(*a*) and 7(*b*) being more distorted than the almost square, Zn-free, four-rings shown in Fig. 7(*c*). Fig. 7(*d*) shows a projection demonstrating the nature of a distorted eight-ring SBU. Fig. 7(*e*) (down [111]) clearly shows the central position of the six rings with the cavities occupied by the K cations (*A* sites); this view clearly shows the distortion of the framework structure and the displacement of K atoms along the large channel. Fig. 7(*f*) shows the equivalent (down [111]) structure for the disordered cubic $Ia\bar{3}d$ $K_2ZnSi_5O_{12}$ leucite and demonstrates the much less distorted structure compared with that for the ordered polymorph (Fig. 7*e*). The structures for the other leucites studied here are not illustrated. There are subtle differences in the degrees of distortions but the structures for hydrothermal monoclinic $P2_1/c$ $K_2FeSi_5O_{12}$ and $K_2CoSi_5O_{12}$ look very similar to those in Figs. 7(*a*)–7(*e*). Similarly, the structures of disordered cubic $Ia\bar{3}d$ $K_2CoSi_5O_{12}$ and $Rb_2MnSi_5O_{12}$ look very similar to that shown in Fig. 7(*f*).

Refined crystallographic parameters allow a more useful analysis of structural changes to be made. Unit-cell parameters for the ordered $P2_1/c$ leucites and for the *Pbca* analogues $Cs_2XSi_5O_{12}$ with *X* = Co and Cd are given in Table 2 and for the disordered $Ia\bar{3}d$ leucites in Table 3; note that the cell volumes for the disordered leucites are all larger than those for the ordered isochemical polymorphs (see below, §3.3). Table 2 gives mean bond lengths for *X*—O, Si—O and *T*—O (*T* = Si and *X*) tetrahedra, for the cavity cation coordinated to the nearest six O atoms ($K—O_6$), and to the full *A*-site polyhedron containing 12 O atoms ($K—O_{12}$) for the hydrothermal ordered $P2_1/c$ leucites with *X* = Mg, Fe, Zn and Co; data for ordered *Pbca* $Cs_2CdSi_5O_{12}$ and $Cs_2CuSi_5O_{12}$ leucites are also

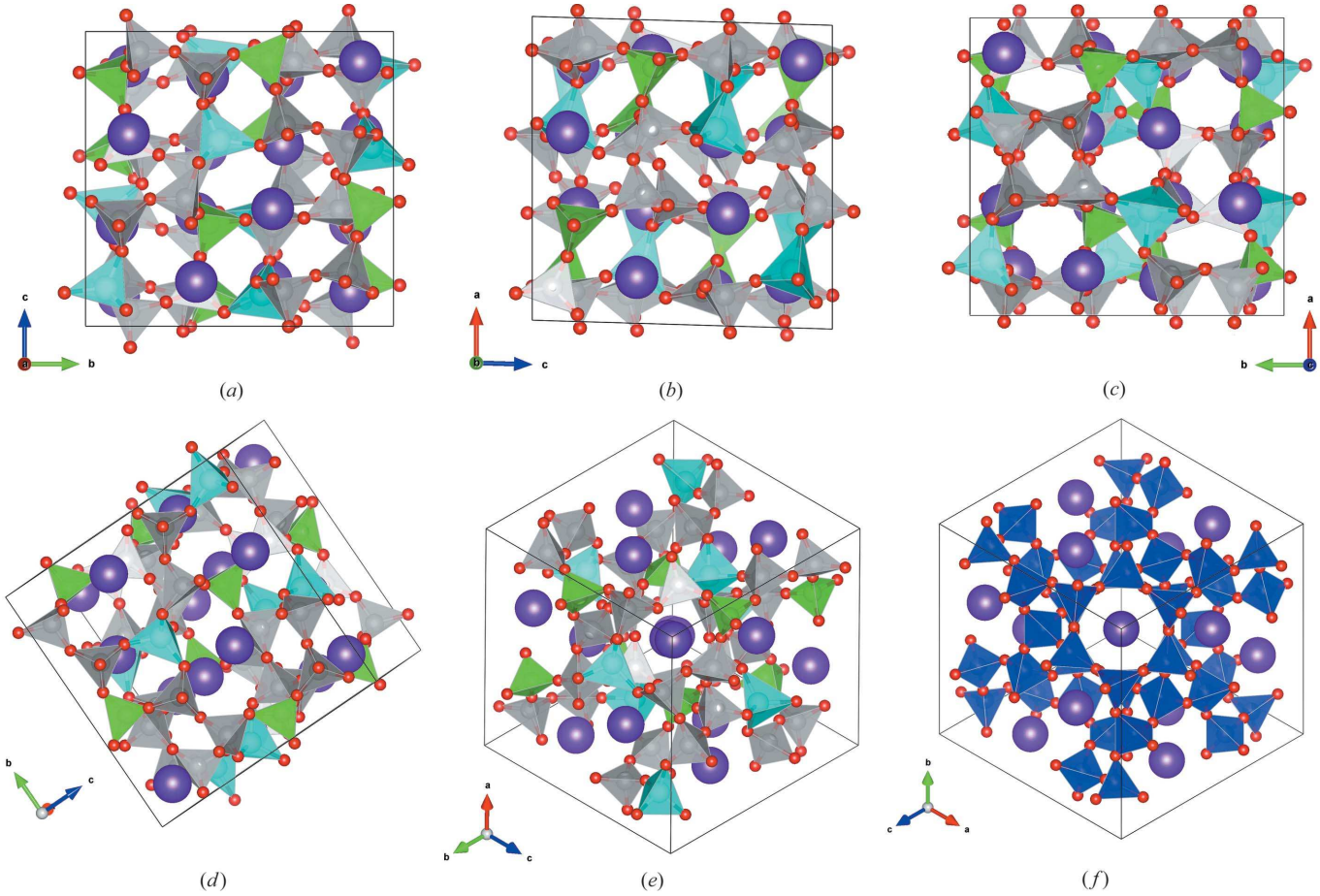

Figure 7
VESTA plots (Momma & Izumi, 2011) showing the crystal structures of hydrothermally and dry-synthesized $K_2ZnSi_5O_{12}$. Figs. 7(*a*)–7(*e*) inclusive show different views of the $P2_1/c$ crystal structure of hydrothermally synthesized $K_2ZnSi_5O_{12}$; purple spheres represent K^+ cations, red spheres represent O^{2-} anions, light-green tetrahedra represent $[Q^4Si(4Si)]$ SiO_4 units, grey tetrahedra represent $[Q^4Si(3Si,1Zn)]$ SiO_4 units and light-blue tetrahedra represent $[Q^4Zn(4Si)]$ ZnO_4 units. Figs. 7(*a*), 7(*b*) and 7(*c*) show the views looking down [100], [010] and [001], respectively. Fig. 7(*d*) shows the labelled tetrahedra of a distorted eight-ring. Fig. 7(*e*) shows the view looking down [111]. Fig. 7(*f*) shows the plot of the $Ia\bar{3}d$ crystal structure of dry-synthesized $K_2ZnSi_5O_{12}$ looking down [111]; purple spheres represent K^+ cations, red spheres represent O^{2-} anions and blue tetrahedra represent disordered $(Si,Zn)O_4$ units.

given for comparison. Table 2 also gives mean intertetrahedral angles Si—O—Si and Si—O—*X* and mean variances (Robinson *et al.*, 1971) for intratetrahedral O—*T*—O angles (*T* = Si, *X*), including mean data for XO_4, $Q^4Si(3Si, 1X)O_4$ and $Q^4Si(4Si)O_4$ tetrahedra. For clarity regarding the detailed linkages between the different tetrahedra we report mean *T*—O—*T* values in Table 4 for all the intertetrahedral angles in the new $P2_1/c$ leucites. Mote that the Q4Si(4Si) atoms occupy the T9 and T12 tetrahedral sites. Bond lengths and bond angles for the $Ia\bar{3}d$ leucites are summarized in Table 3.

3.2. Bond-length variations for *T*—O and *A*—O distances

The mean Si—O bond lengths in the ordered $P2_1/c$ leucites are in the range 1.61–1.63 Å, slightly higher than found in silica frameworks (quartz and tridymite) but match the Si—O bond lengths reported for ordered Si sites in aluminosilicates (*e.g.* feldspars and feldspathoids) (*e.g.* Smyth & Bish, 1988). In addition, the mean bond length for the $Q^4Si(4Si)$ unit is slightly smaller than for the overall mean Si—O, which in turn must be slightly smaller than that for the $Q^4Si(3Si,1X)$ tetrahedra. Thus, the presence of divalent cations in ordered leucite frameworks does not significantly disturb the Si—O environment typical of polymerized silicate frameworks. The mean *X*—O distances range from 1.89 to 1.96 Å, close to the EXAFS first-shell values for similar leucites (Mg—O 1.93; Fe^{2+}—O 1.99; Co—O 1.96; Zn—O 1.93 Å) reported by Henderson *et al.* (2016). These values are close to the calculated Mg—O, Fe^{2+}—O, and Co—O distances obtained from Shannon (1976) ionic radii using an O^{2-} ionic radius of 1.35 Å for two-coordinated O in a fully polymerized $T—O_4$ framework (Mg—O 1.92; Fe^{2+}—O 1.98; Co—O 1.93 Å). However, the mean Zn—O distance of 1.89 Å for the $K_2ZnSi_5O_{12}$ sample is anomalously low (*cf.* 1.95 Å; Shannon, 1976) and it is possible that there is some Si–Zn disorder in the *T* sites as found for the $Cs_2ZnSi_5O_5$ sample which has the orthorhombic *Pbca* space group (Bell & Henderson, 2009). Table 2 gives the mean K—O bond lengths for the six-nearest O atoms (K—O_6) as well as for the full 12-fold polyhedron (K—O_{12}); the mean values for K—O_6 range from 3.00 to 3.06 Å [mean 3.02 (2) Å] and for K—O_{12} range from 3.31 to 3.36 Å (Table 2). Also given in Table 2 are the calculated K—O_6 and K—O_{12} bond distances obtained using equation 10 in Henderson *et al.* (2017); these show good agreement with the experimental data reported here. The K—O_6 distances reported in Table 2 match those found for natural aluminosilicate $KAlSi_2O_6$ leucites (3.00–3.01 Å; Mazzi *et al.*, 1976; Gatta *et al.*, 2008*b*; Palmer *et al.*, 1997), for synthetic $KFe^{3+}Si_2O_6$ (3.01–3.02 Å; Palmer *et al.*, 1997; Bell & Henderson, 1994), and for synthetic $KBSi_2O_6$ leucites (3.00–3.05 Å; Martucci *et al.*, 2011; Mikloš *et al.*, 1992). All of these six-oxygen values are close to a Shannon (1976) distance of 3.02 Å for 12-coordinated K. Indeed, Gatta *et al.* (2008*b*) considered that in natural leucite the theoretical coordination of K is nine at 0.0001 GPa. Thus, the longer K—O bonds found in the *A*-site polyhedron lead to the bond valence sums for all 12 O atoms being significantly <1 which points to significant underbonding of the cavity cations (K, Rb and Cs) in leucite-type structures in general (Henderson *et al.*, 2017).

The structural parameters for the disordered $Ia\bar{3}d$ leucites (Table 3) are less complicated as this space group contains a single tetrahedral site, a single *A* site, and only two distinct O atoms. The mean *T*—O bond length for the single *T* site ranges from 1.61 to 1.65 Å and in each case is smaller (by from 0.02 to 0.06 Å) than the mean *T*—O distance for the equivalent ordered isochemical polymorph; despite this difference the unit-cell volumes of the disordered polymorphs are larger than those for their ordered equivalents (see below, §3.3). The *A*—O distances split into two sets of six; the nearest six O atoms have fixed values ranging from 3.30 to 3.36 Å for the different samples and show little systematic change depending on whether the cavity cation is relatively small K, intermediate Rb or larger Cs. Note that the $K_2X\,Si_5O_{12}$ samples all have significantly longer K—O_6 distances than the Shannon (1976) bond distance expected for 12-coordination (K—O = 3.02 Å), the $Rb_2MnSi_5O_{12}$ sample has a Rb—O_6 leucite value matching the Shannon value of 3.07 Å, and the cubic $Cs_2CuSi_5O_{12}$ leucite has a Cs—O_6 value significantly shorter than the Shannon value (3.22 Å). The oxygen positions for the $Cs_2CuSi_5O_{12}$ leucite should be very reliable as this sample was studied mainly by neutron diffraction so this relationship is likely to be robust. The fixed distances for the second set of six O atoms around the *A* cation are even longer and give mean *A*—O_{12} values for the full 12-coordinated polyhedron in the range 3.31–3.45 Å; indeed if the value for the *X* = Co sample is disregarded, the other $K_2XSi_5O_{12}$ leucites and the $Rb_2MnSi_5O_{12}$ sample all effectively have the same *A*—O_6 distance of 3.41 Å, with the Cs—O_{12} distance being only slightly longer (3.45 Å). All the mean *A*—O_{12} distances are much longer than the expected Shannon 12-coordinated oxygen polyhedra. It seems that for the disordered $Ia\bar{3}d$ leucites the sizes of the large channels hosting the *A* sites are controlled by the intrinsic properties of the framework rather than being controlled by the collapse of the framework about the species of cavity cation present in this site. Alternatively, it could be commented that the constraints of the adopted space group do not adequately allow the geometry of the alkali polyhedra to be represented reliably.

3.3. Bond-angle variations for intratetrahedral (O—*T*—O) and intertetrahedral (*T*—O—*T*) angles

The structural positions of the O atoms in the samples are most reliably determined using neutron diffraction (see earlier) and we use our published data for *Pbca* $Cs_2CuSi_5O_{12}$ (Bell *et al.*, 2010) to establish the trends for the distortions of the different ordered tetrahedral sites. Thus, the data for this compound (Table 2) show that the mean tetrahedral angle variance [σ^2; Robinson *et al.* (1971)] is smallest (19.1 deg^2) for the Q4Si(4Si) site, which reflects the fact that this site has the most symmetrical local environment in the framework. The mean variance for the $Q^4Si(3Si,1Cu)$ site is significantly larger (38.1 deg^2), as expected, as one of the next-nearest neighbours (NNN) is a CuO_4 tetrahedron. Also, as expected, the longer

weaker Cu—O bonds in the Q^4Cu (4Si) tetrahedron lead to a much larger variance of 159 deg^2. The mean O—Si—O and T—O—T variances (also shown in Table 2) reflect these differences. The synchrotron X-ray data for $P2_1/c$ $K_2MgSi_5O_{12}$ and $Pbca$ $Cs_2CdSi_5O_{12}$ (Table 2) show exactly the same geometric relations even though the O atom positions will be less reliable than for neutron diffraction data. However, note that the variances for the MgO_4 and CdO_4 tetrahedra are much smaller than that for CuO_4 (40.4, 94.2 and 159.4 deg^2, respectively) which might be related to the local Cu environment also being modified by Jahn–Teller effects. The laboratory X-ray data for the three $P2_1/c$ $K_2XSi_5O_{12}$ leucites (for X = Fe, Co and Zn) generally show these same trends except that the variance for the mean Q^4Si(4Si) site in the $K_2FeSi_5O_{12}$ sample is slightly larger than that for Q^4Si(3Si, 1Fe); it is likely that this reflects experimental error on oxygen atomic coordinates. Although the very high variance for the Q^4Fe(4Si) might be anomalous, the presence of transition elements with electron vacancies in the 3d shell is accompanied by consistently higher tetrahedral angle variances (*e.g.* Cu, Fe, Co; Table 2) and also for Mn (Bell & Henderson, 2016). The data for all of the ordered leucites (Table 2 and Bell & Henderson, 1996, 2009, 2016) show that the mean O—T—O tetrahedral variance for MgO_4 in $K_2MgSi_5O_{12}$ has the smallest value determined.

The intertetrahedral T—O—T angle data for the different T sites in the new ordered samples are given in Table 4 and the average values for different tetrahedral species are summarized in Table 2. Note that a Q^4Si(4Si) tetrahedron in a four-ring SBU is only linked to one species of NNN [*i.e.* Q^4Si(3Si, 1Cu) tetrahedra], thus, only one value is given for the mean Si—O—Si linkage. The XO_4 tetrahedral unit is always linked to two NNN Q^4Si(3Si, 1X) tetrahedra and only one mean Si—O—X angle is reported. In all leucite compounds, the Si—O—X angles are significantly smaller than those for Si—O—Si and this reflects the presence of weaker X—O bonds in these tetrahedral units which in turn leads to easier collapse of the framework around the cavity cations. Note also that the ordered $K_2XSi_5O_{12}$ leucites with X = Fe and Co have mean X—O distances longer than that for Mg—O but they both have unit-cell volumes smaller than that for the X = Mg compound, which is presumably related to the greater collapse of frameworks with longer, weaker Fe—O and Co—O bonds. Although the X = Zn sample has a Zn—O bond length not significantly different to that for Mg—O, its unit-cell volume is also smaller than that for the X = Mg sample, consistent with the presence of weaker Zn—O bonds.

The mean O—T—O and T—O—T bond angles for the disordered $Ia\bar{3}d$ cubic $K_2XSi_5O_{12}$ leucites are given in Table 3, where they are also compared with the data for the $Ia\bar{3}d$ $Rb_2MnSi_5O_{12}$ (this work) and $Cs_2CuSi_5O_{12}$ (Bell *et al.*, 2010) analogues. The tetrahedral angle variance for the disordered Si+Mg sample is very low (10.7 deg^2) and the same as that for disordered Si+Zn; the variances are much higher for the disordered Si + Co, Mn or Cu samples. The mean T—O bond lengths for the $Ia\bar{3}d$ $K_2MgSi_5O_{12}$ and $K_2ZnSi_5O_{12}$ samples are identical and smaller than those for the Co, Mn and Cu equivalents; by contrast, the mean T—O—T angles for the $K_2MgSi_5O_{12}$ and $K_2ZnSi_5O_{12}$ samples are larger than those for the $K_2CoSi_5O_{12}$, $Rb_2MnSi_5O_{12}$ and $Cs_2CuSi_5O_{12}$ leucites (Table 3). In addition, the T—O—T angles for the disordered $Ia\bar{3}d$ leucites (Table 4) are all larger than the mean T—O—T angle for the ordered polymorphs (Table 2; T—O—T for ordered $Rb_2MnSi_5O_{12}$ = 136.8°). We have shown earlier that the disordered polymorphs always have higher cell volumes than their isochemical ordered equivalents and this matches their larger T—O—T angles; both of these features point to a larger framework for the disordered leucites. Thus, the statistical distribution of Si and X cations in the disordered leucites clearly leads to a 'stiffer' framework which is less susceptible to collapse about the cavity cations; indeed, the anomalously long K—O_6 bond lengths in all the $Ia\bar{3}d$ $K_2XSi_5O_{12}$ leucites are consistent with the framework collapse around the A-site cavity being unable to reach a sterically sensible K—O polyhedron.

3.4. T—O distance *versus* T—O—T angle relationships

It is clear that both the ordered and disordered leucites display an inverse relationship between T—O bond lengths and T—O—T angles; this is a well known relationship shown by the framework structures of SiO_2 polymorphs, alkali/alkaline earth aluminosilicates, aluminates and phosphates (*e.g.* Brown *et al.*, 1969; Brown & Gibbs, 1970; Taylor, 1972; Hill & Gibbs, 1979). Note that Si—O bonds in pure SiO_2 compounds [O coordination number (CN) = 2] are slightly smaller (~0.02 Å) than those in aluminosilicates (O CN > 2); this is the same relationship we find in our ordered leucites. Brown *et al.* (1969) correlated trends for Si—O bond lengths *versus* Si—O—Si angles in SiO_2 and aluminosilicates with the replacement of Si in the tetrahedral framework by the more electropositive Al. Brown & Gibbs (1970) also showed that minerals with Si-rich tetrahedra have larger T—O—T angles than those with Al-, Mg-, B- and Be-rich tetrahedra. These relationships are similar to those we find in our ordered and disordered leucite analogues.

Fig. 8 shows the relationship between mean T—O bond lengths [for T = Q^4Si(4Si), all Q^4Si, and Q^4X(4Si)] *versus* the equivalent mean T—O—T angles for all the reliable data for our ordered and disordered leucites with the stoichiometry $A_2XSi_5O_{12}$ (Bell *et al.*, 1994*a*,*b*, 2010; Bell & Henderson, 1994, 1996, 2009, 2016). In particular, note that the relationship between mean intertetrahedral Si—O—Si angles and mean Si—O distances are shown for linkages involving the Q^4Si(4Si) tetrahedra [*i.e.* Q^4Si(4Si)—O—Q^4Si(3Si, 1X)] and those for the Q^4Si(3Si, 1X)—O—Q^4Si(3Si, 1X) angles (see Table 2). The linear regression equation for the mean values for the latter is

$$\text{Si—O—Si angle} = 2.155 - 0.0038 * \text{Si—O distance} \quad (R\text{-factor} = 0.73).$$

The points defining the mean for the Q^4Si(4Si) tetrahedra alone fall close to this set, as do the data for the cubic, $Ia\bar{3}d$, disordered leucites (Fig. 8). The data for the mean inter-

tetrahedral angles between the $Q^4X(3Si, 1X)$ tetrahedra and the adjacent $Q^4Si(3Si, 1X)$ tetrahedra are also plotted *versus* mean $X-O$ distance in Fig. 8 and define a scattered region with longer $T-O$ distances and smaller $T-O-T$ angles than the Si tetrahedra. The regression fit for these data is:

$$Q^4Si(3Si, 1X)-O-Q^4X(3Si, 1X) \text{ angle} = 3.798 - 0.0141 * X-O \quad (R\text{-factor} = 0.49).$$

The steeper slope for the relationship for the X tetrahedra is largely controlled by the data for the $Rb_2CdSi_5O_{12}$ and $Cs_2CdSi_5O_{12}$ samples. The very different crystal chemical properties of Mg and Cd compared with those for the 3*d* transition elements lead to the scattered relationship shown. However, it is clear the combination of the data for the Si tetrahedra bond distances and bond angles with those for the X tetrahedra data defines a very clear inverse relationship which gives the regression equation:

$$T-O-T \text{ angle} = 5.037 - 0.0239 * T-O \text{ distance} \quad (R\text{-factor} = 0.88;\ T = Q^4Si \text{ or } Q^4X).$$

The fact that these very different tetrahedral units exist in the same framework topology underlines the extreme flexibility of the leucite structure and the fact that both ordered and disordered polymorphs occur for $K_2XSi_5O_{12}$ (X = Mg, Co, Zn), $Rb_2MnSi_5O_{12}$ and $Cs_2CuSi_5O_{12}$ analogues reinforces this observation. The equivalent data for the pseudocubic cell for the ordered leucites (obtained by averaging the data for the Si and X sites) and the overall $T-O-T$ *versus* $T-O$ trend are shown in Fig. 9. The disordered $Ia\bar{3}d$ samples are also plotted in this figure and are displaced to higher $T-O-T$ angles and lower $T-O$ bond distances than the averaged data for the ordered samples. The regression line fitted for all of the data shown in Fig. 9 defines the equation:

$$T-O-T \text{ angle} = 2.864 - 0.0086 * T-O \text{ distance} \quad (R = 0.813).$$

These data also show a clear inverse relationship between $T-O-T$ and $T-O$.

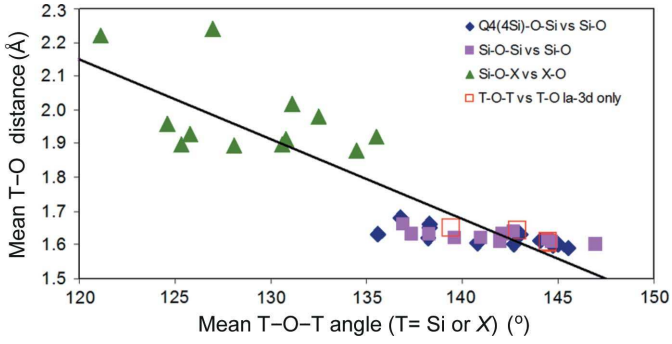

Figure 8
The relationship between mean $T-O$ bond length and corresponding mean $T-O-T$ angle for all our reliable data for ordered and disordered leucites with the stoichiometry $A_2XSi_5O_{12}$ (Bell *et al.*, 1994*a*,*b*, 2010; Bell & Henderson, 1996, 2009, 2016).

We have used the multivariant linear regression technique in an attempt to derive more satisfactory regression equations than the simple equations obtained using the measured $T-O-T$ and only one measured ($T-O$); thus for the multivariant regression models the dependent variable ($T-O-T$) is fitted using dependent variable ($T-O$) with addition of other independent variables (*e.g.* cavity cation size, tetrahedral angle variance, X cation electronegativity). This approach provided some improvements as shown by the best multivariant regression equations in Table 5. Following the approach of Henderson *et al.* (2017) we have attempted to simplify the use of such equations to predict crystal chemical properties for the leucites by using standard Shannon (1976) ionic radii for 12-coordinated alkali cations rather than the determined $A-O_6$ or $A-O_{12}$; we also used mean tetrahedral ionic radii for tetrahedral cations (Shannon) as a possible independent variable rather than measured $T-O$. Equation (1) (Table 5) defines the simple relationship between mean $Si-O-Si$ angle and mean $Si-O$ distance (R-factor = 0.728); the 'null hypothesis significance' parameters for the $Si-O$ independent variable is 0.007 showing that there is an 0.7% probability of the calculated variations being random. Adding the Shannon cavity cation radii for K, Rb or Cs gave a small improvement [Table 5, equation (2) (R-factor 0.746)] but note that the significance for this term is very low (~50% possible error). Addition of other independent variables including mean $X-O$ distance, Shannon mean tetrahedral ionic radius radii, intertetrahedral angle variance, and bond strength did not improve the fit. However, using the data for the mean $Q^4Si(4Si)-O$ tetrahedral distance did show significant improvement [equations (3) and (4)]. Equation (4) (R-factor = 0.891) is the most reliable equation for the $Si-O-Si$ relationship but note that the parameter for the cavity radius has an uncertainty of ~1.4% and that for the tetrahedral angle variance has an uncertainty of ~4%. The relationship for $Q^4Si(4Si)-O-Si$ (R = 0.887) is also reasonably well defined but has an uncertainty of ~2% for the cavity cation term.

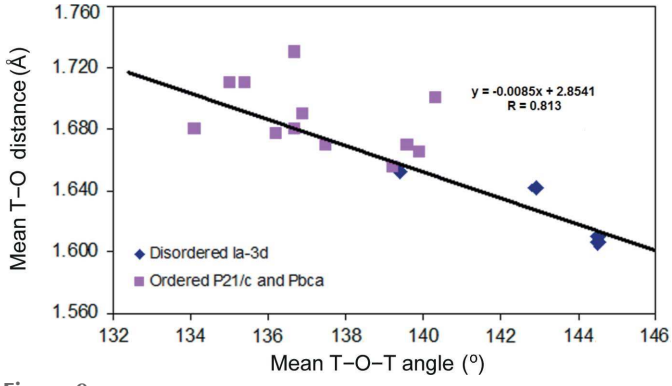

Figure 9
The relationship between mean $T-O$ bond length and corresponding mean $T-O-T$ angle for the pseudocubic cell for the ordered leucites (obtained by averaging the data for the Si and X sites) with the stoichiometry $A_2XSi_5O_{12}$ (Bell *et al.*, 1994*a*,*b*, 2010; Bell & Henderson, 1996, 2009, 2016).

Table 5
Regression equations showing the relationships between T—O interatomic distances (Å) and T—O—T interatomic angles (°).

Equation No.	Dependent variable	R	Standard error of estimate	F factor	Intercept	Si—O (Å)	Q^4Si—O (Å)	X—O (Å)	T—O (Å)	Cavity cation ideal radius	Variance O—Si—O (°)	Electronegativity Pauling
						a†	b†	c†	d†	e†	f†	g†
(1)	Si—O—Si	0.728	2.21	5.43	371.1	−141.4						
(2)	Si—O—Si	0.746	2.26	5.66	373.3	−147.7				+4.59		
(3)	Si—O—Si	0.818	1.95	9.11	286.3		−102.9			+12.7		
(4)	Si—O—Si	0.891	1.63	10.2	326.5		−133.2			+16.9	+0.016	
(5)	Q^4Si—O—Si	0.717	2.57	10.6	399.7	−159.3						
(6)	Q^4Si—O—Si	0.775	2.33	15.0	300.5		−98.2					
(7)	Q^4Si—O—Si	0.887	1.79	16.6	320.9		−127.7			+15.6		
(8)	Si—O—X	0.918	2.01	14.3	138.2			−24.6		+31.8		−9.51
(9)	T—O—T	0.642	1.73	3.16	197.8				−45.4	+9.11		
(10)	T—O—T	0.851	1.26	7.03	316.4	−112.6		−9.38		+12.7		

† Multivariant linear equations for dependent variable T—O—T (°) are of the form: intercept + a*(SiO) + b*(Q4Si—O) + c*(X—O) + d*(T—O) + e*(cavity cation radius) + f*(O—T—O variance) + g*(electronegativity).

Fitting the relationship for the X—O—Si angles is much more difficult resulting from the large range of X ionic radii and bond properties, but using the independent variables X—O distance, cavity cation size and electronegativity value (Pauling, 1960) gave a satisfactory fit with equation (8) (Table 5) but note that the electronegativity regression term has an uncertainty of ∼2.4% (the other parameters have uncertainties ∼1%). For the averaged T—O—T *versus* T—O fits the best regression fit achieved is equation (10) (Table 5) (R = 0.851) which has uncertainties of ∼0.4% for the Si—O term, ∼3.3% for X—O and ∼0.9% for the cavity cation size.

The correspondence of the measured and calculated inter-tetrahedral angles is displayed in Fig. 10 which shows data from equation (4) [Si—O—Si *versus* Q^4Si(4Si)—O], equation (7) [Q^4Si(4Si)—O—Q^4Si(3Si, 1X) *versus* Q^4Si(4Si)—O], equation (10) (T—O—T *versus* T—O), and equation (8) [Q^4Si(3Si, 1X)—O—X *versus* X—O]. The points from equations (4) and (7) fall in the same region confirming that both species of ordered Si—O_4 units give similar answers; the T—O—T data falls on the same trend, partially overlapping the ordered Si tetrahedral data and, as expected, the Si—O—X angles are displaced to lower angles consistent with those samples have the relatively large divalent cations replacing smaller Si ordered into separate sites. The data point for *Pbca* $Rb_2MnSi_5O_{12}$ obtained from equations (7) and (8) (Table 5) plot slightly away from the main trend suggesting that the oxygen data for this sample are less reliable than those for the other samples.

3.5. Possible displacive phase transitions ($P2_1/c \rightarrow Pbca$) in $K_2XSi_5O_{12}$ (X = Fe, Zn, Co) leucite analogues

Monoclinic space group $P2_1/c$ is a maximal subgroup of orthorhombic *Pbca* and should show a phase transition with *Pbca* having the same types of sites but halved in number, namely two Q^4Si(4Si), two Q^4X(4Si), eight Q^4Si(3Si, 1X) pfu in $P2_1/c$ and one Q^4Si(4Si), one Q^4X(4Si), four Q^4Si(3Si, 1X) pfu in *Pbca*. Redfern & Henderson (1996) confirmed that ordered $P2_1/c$ $K_2MgSi_5O_{12}$ leucite shows this transition to the high-temperature *Pbca* polymorph at 622 K *via* a reversible, first-order ferroelastic phase transition; the first-order character was attributed to a large excess volume which results from collapse of the framework around the large cavity cation site occupied by the alkali element. It seems inevitable that the new $P2_1/c$ leucites reported here will also show this type of transition at elevated temperature.

Based on the tetrahedral site connectivities summarized in Table 4 and the data reported in the supporting information, it is clear the tetrahedral sites 5 and 6 are occupied by the X cation, while sites 9 and 12 are occupied by the Q^4Si(4Si) species. During the phase transition these two pairs will merge to form a single site for each type. Using the tetrahedral site notation for *Pbca* (Bell *et al.*, 1994*b*; 2010) tetrahedral site 1 is occupied by X and site 2 by Q^4Si(4Si). Thus, $P2_1/c$ X sites 5 and 6 merge to form *Pbca* site 1 and Q^4Si(4Si) sites 9 and 12 will merge to form *Pbca* site 2. The merger of the other Si sites Q^4Si(3Si,1X) follows but an error in Bell *et al.* (1994*b*, Fig. 2) duplicates sites 3 and 11 and omits sites 4 and 7. This error is

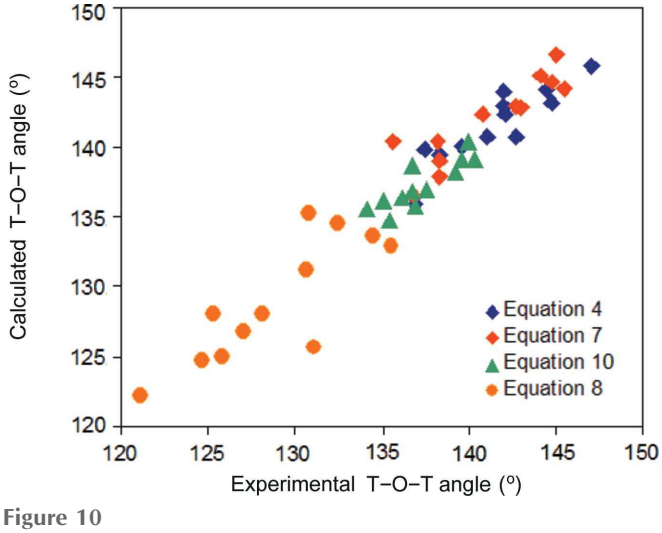

Figure 10
The relationships between measured and calculated T—O—T angles.

Table 6
Site assignments for $P2_1/c$ to *Pbca* phase transition.

	$P2_1/c$ central atom		$P21/c$ connected to				*Pbca*
Tetrahedral site	Label	Type					Label
*T*1	Si1	Q^4Si(3Si,1*X*)	Si4	Si8	Si12	*X*6	*T*5 (Si)
*T*2	Si2	Q^4Si(3Si,1*X*)	Si3	Si11	Si9	*X*5	
*T*3	Si3	Q^4Si(3Si,1*X*)	Si2	Si7	Si12	*X*5	*T*6 (Si)
*T*4	Si4	Q^4Si(3Si,1*X*)	Si1	Si10	Si9	X6	
*T*5	X5	Q^4X(4Si)	Si2	Si3	Si10	Si11	*T*1 (*X*)
*T*6	*X*6	Q^4X(4Si)	Si1	Si4	Si7	Si8	
*T*7	Si7	Q^4Si(3Si,1*X*)	Si3	Si11	Si12	*X*6	*T*3 (Si)
*T*10	Si10	Q^4Si(3Si,1*X*)	Si4	Si8	Si9	X5	
*T*8	Si8	Q^4Si(3Si,1*X*)	Si1	Si10	Si9	*X*6	*T*4 (Si)
*T*11	Si11	Q^4Si(3Si,1*X*)	Si2	Si7	Si12	*X*5	
*T*9	Si9	Q^4Si(4Si)	Si2	Si4	Si8	Si10	*T*2 (Si)
*T*12	Si12	Q^4Si(4Si)	Si1	Si3	Si7	Si11	

corrected in Redfern & Henderson (1996) but to clarify matters here we show the actual linkages in Table 6. Bell *et al.* (1994*a*) pointed out that sites Si3 and Si11 in $K_2MgSi_5O_{12}$ are linked to the same set of NNN atoms (Si2, Si7, Si12 and Mg5) while Si4 and Si8 are both linked to Si1, Si9, Si10 and Mg6 (see our Table 6). However, during the phase transition, Si 3 and Si 11 could not merge into a single site and neither could Si4 and Si8 as that would leave Si9 and Si12 as separate Q^4Si(4Si) sites and Mg5 and Mg6 as separate Q^4Mg(4Si) sites. It is clear that the merging sites must have different NNN atom species; thus Si 1 must link with Si2 rather than Si10, and Si3 must link with Si4 rather than Si8. This can only leave Si7 to link to Si10 and Si8 to Si11 as shown by Redfern & Henderson (1996; see our Table 6).

To assess the possible phase transition relationships we adopt the model of Henderson *et al.* (2017) to describe the structural relations in terms of a 'pseudocubic' $Ia\bar{3}d$ unit cell. Thus in Fig. 11 we show the relationship between the pseudocubic cell edges ($V^{1/3}$) and measured mean $A-$O bond lengths to the nearest six O atoms ($A-O_6$). Also shown are the calculated $A-O_6$ bond lengths for the $A_2MgSi_5O_{12}$ (A = K, Rb, Cs) analogues at room temperature and for the high-temperature $K_2MgSi_5O_{12}$ leucite unit-cell measurements (Redfern & Henderson, 1996); the calculated data were obtained using equation (9) from Henderson *et al.* (2017). All of the points below a cubic cell edge of 13.45 Å have the spacegroup $P2_1/c$ and those above this cell edge are for *Pbca* analogues. For the room-temperature data, the measured trends for the $A-O_6$ (A = K, Rb, Cs) bond length *versus* pseudocubic cell edge are very close for X = Mg and Zn analogues but that for $A_2CoSi_5O_{12}$ leucites (A = K, Rb, Cs) appears to be slightly shallower. We do not have data for $Rb_2FeSi_5O_{12}$ or $Cs_2FeSi_5O_{12}$ samples. The calculated $K-O_6$ *versus* pseudocell edge trend for the $K_2MgSi_5O_{12}$ leucite thermal expansion experiments (Redfern & Henderson, 1996) lies below that of the measured $K_2MgSi_5O_{12}$ and $Rb_2MgSi_5O_{12}$ samples at room temperature with a slightly smaller slope (but note that the calculated K—O distance matches that reported by Redfern and Henderson at room temperature). The values for the *Pbca* $K_2MgSi_5O_{12}$ leucite at 709 K are slightly lower than the measured values for $Rb_2MgSi_5O_{12}$ leucite at room temperature. It is well known that anisotropic thermal motion of O atoms in framework structures results in bond length shortening (Taylor, 1972; Hill & Gibbs, 1979) leading to volume decrease and it is likely that the crystallographic parameters for $Rb_2MgSi_5O_{12}$ leucite at room temperature are close to the critical values required to stabilize a $P2_1/c$ to *Pbca* phase transition. The measured cell parameters and $K-O_6$ distances for $K_2Fe^{2+}Si_5O_{12}$, $K_2ZnSi_5O_{12}$ and $K_2CoSi_5O_{12}$ $P2_1/c$ leucites all plot close to those for $K_2MgSi_5O_{12}$ leucite but with slightly smaller values. We speculate, therefore, that all of these samples should show phase transitions to *Pbca* at temperatures close to 700 K. We hope to be able to carry out heating experiments on these samples with structure determinations at key temperatures which would provide the data necessary for characterizing the geometric changes occurring during the phase transitions.

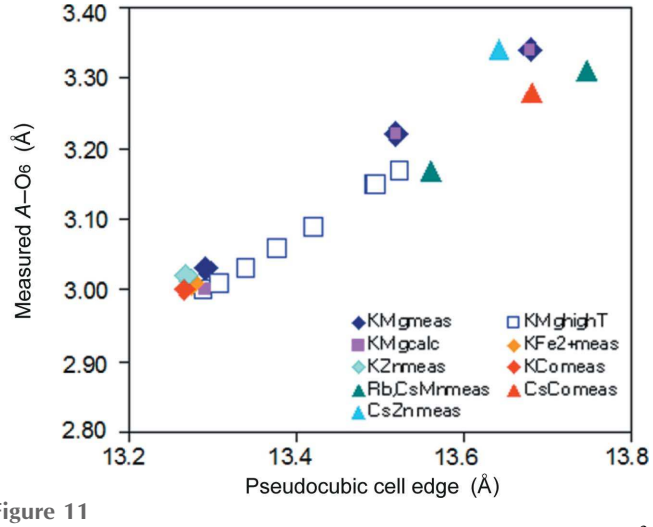

Figure 11
The relationships between the $A-$O bond lengths for the nearest six O^{2-} anions and the 'pseudocubic' ($V^{1/3}$) lattice parameters for $A_2XSi_5O_{12}$, where A = K^+, Rb^+, Cs^+ and X = Mg^{2+}, Fe^{2+}, Co^{2+}, Zn^{2+}. See text for discussion about the probable phase transitions from $P2_1/c$ to *Pbca* structures at elevated temperatures. Calculated comparative data were obtained using equation (9) given by Henderson *et al.* (2017).

4. Conclusions

$P2_1/c$ crystal structures have been refined for the hydrothermally synthesized leucite tectosilicate mineral analogues $K_2X^{2+}Si_5O_{12}$ (X = Fe^{2+}, Co, Zn). These structures are isostructural with the $P2_1/c$ crystal structure of hydrothermally synthesized $K_2MgSi_5O_{12}$ (Bell *et al.*, 1994*a*). $Ia\bar{3}d$ crystal structures have been refined for the dry-synthesized leucite tectosilicate mineral analogues $K_2X^{2+}Si_5O_{12}$ (X = Co, Zn) and $Rb_2X^{2+}Si_5O_{12}$ (X = Mn) structures. These structures are isostructural with the $Ia\bar{3}d$ crystal structure of dry-synthesized $K_2MgSi_5O_{12}$ (Bell *et al.*, 1994*a*).

Analyses of the tetrahedral ($T-$O) bond lengths and intertetrahedral ($T-$O$-T$) bond angles for these and other leucite structures show a clear inverse relationship between $T-$O$-T$ and $T-$O.

Acknowledgements

We wish to acknowledge the use of the EPSRC funded National Chemical Database Service hosted by the Royal Society of Chemistry.

References

Agakhanov, A. A., Pautov, L. A., Karpenko, V. Yu., Sokolova, E. & Hawthorne, F. C. (2012). *Can. Mineral.* **50**, 523–529.
Baerlocher, Ch., Meier, W. M. & Olson, D. H. (2001). *Atlas of Zeolite Framework Types.* Structure Commission of the International Zeolite Association, 5th edition. Amsterdam: Elsevier.
Bell, A. M. T. & Henderson, C. M. B. (1994). *Acta Cryst.* C**50**, 1531–1536.
Bell, A. M. T. & Henderson, C. M. B. (1996). *Acta Cryst.* C**52**, 2132–2139.
Bell, A. M. T. & Henderson, C. M. B. (2009). *Acta Cryst.* B**65**, 435–444.
Bell, A. M. T. & Henderson, C. M. B. (2016). *Acta Cryst.* E**72**, 249–252.
Bell, A. M. T., Henderson, C. M. B., Redfern, S. A. T., Cernik, R. J., Champness, P. E., Fitch, A. N. & Kohn, S. C. (1994*b*). *Acta Cryst.* B**50**, 31–41.
Bell, A. M. T., Knight, K. S., Henderson, C. M. B. & Fitch, A. N. (2010). *Acta Cryst.* B**66**, 51–59.
Bell, A. M. T., Redfern, S. A. T., Henderson, C. M. B. & Kohn, S. C. (1994*a*). *Acta Cryst.* B**50**, 560–566.
Brown, G. E. & Gibbs, G. V. (1970). *Am. Mineral.* **55**, 1587–1607.
Brown, G. E., Gibbs, G. V. & Ribbe, P. H. (1969). *Am. Mineral.* **54**, 1044–1061.
Ferraris, G., Jones, D. W. & Yerkess, J. (1972). *Z. Kristallogr.* **135**, 240–252.
Finger, L. W., Cox, D. E. & Jephcoat, A. P. (1994). *J. Appl. Cryst.* **27**, 892–900.
Gatta, G. D., Rotiroti, N., Ballaran, T. B. & Pavese, A. (2008*b*). *Am. Mineral.* **93**, 1588–1596.
Gatta, G. D., Rotiroti, N., Fisch, M., Kadiyski, M. & Armbruster, T. (2008*a*). *Phys. Chem. Mineral.* **35**, 521–533.
Henderson, C. M. B., Bell, A. M. T. & Knight, S. K. (2017). *J. Solid State Chem.* **251**, 90–104.
Henderson, C. M. B., Bell, A. M. T., Kohn, S. C. & Page, C. S. (1998). *Mineral. Mag.* **62**, 165–178.
Henderson, C. M. B., Charnock, J. M., Bell, A. M. T. & van der Laan, G. (2016). *J. Non-Cryst. Solids*, **451**, 23–48.
Hill, R. J. & Gibbs, G. V. (1979). *Acta Cryst.* B**35**, 25–30.
Laar, B. van & Yelon, W. B. (1984). *J. Appl. Cryst.* **17**, 47–54.
Martucci, A., Pecorari, P. & Cruciani, G. (2011). *Microporous Mesoporous Mater.* **142**, 570–576.
Mazzi, F., Galli, E. & Gottardi, G. (1976). *Am. Mineral.* **61**, 108–115.
Mikloš, D., Smrčok, Ľ., Ďurovič, S., Gyepesová, D. & Handlovič, M. (1992). *Acta Cryst.* C**48**, 1831–1832.
Momma, K. & Izumi, F. (2011). *J. Appl. Cryst.* **44**, 1272–1276.
Palmer, D. C., Dove, M. T., Ibberson, B. M. & Powell, B. M. (1997). *Am. Mineral.* **82**, 16–29.
PANalytical (2009). *High Score Plus* (v.2.2.1). PANalytical, Almelo, The Netherlands.
Pauling, L. (1960). *The Nature of the Chemical Bond.* Cornell University Press.
Redfern, S. A. T. & Henderson, C. M. B. (1996). *Am. Mineral.* **81**, 369–374.
Redhammer, G. J. & Roth, G. (2002). *Am. Mineral.* **87**, 1464–1476.
Rietveld, H. M. (1969). *J. Appl. Cryst.* **2**, 65–71.
Robinson, K., Gibbs, G. V. & Ribbe, P. H. (1971). *Science*, **172**, 567–570.
Rodríguez-Carvajal, J. (1993). *Physica B*, **192**, 55–69.
Shannon, R. D. (1976). *Acta Cryst.* A**32**, 751–767.
Smyth, J. R. & Bish, D. L. (1988). *Crystal Structures and Cation Sites of the Rock-Forming Minerals.* Allen and Unwin.
Taylor, D. (1972). *Mineral. Mag.* **38**, 629–631.
Thompson, S. P., Parker, J. E., Potter, J., Hill, T. P., Birt, A., Cobb, T. M., Yuan, F. & Tang, C. C. (2009). *Rev. Sci. Instrum.* **80**, 075107.
Torres-Martinez, L. M. & West, A. R. (1989). *Z. Anorg. Allg. Chem.* **573**, 223–230.
Yanase, I., Kobayashi, H., Shibasaki, Y. & Mitamura, T. (1997). *J. Am. Ceram. Soc.* **80**, 2693–2695.